



University of  
Massachusetts  
Amherst

## Interplay Between Ion Transport, Applied Bias and Degradation under Illumination in Hybrid Perovskite p-i-n Devices

Item Type	article;article
Authors	Smith, Emily C.
DOI	<a href="https://doi.org/10.1021/acs.jpcc.8b01121">https://doi.org/10.1021/acs.jpcc.8b01121</a>
Rights	UMass Amherst Open Access Policy
Download date	2024-08-06 18:21:13
Link to Item	<a href="https://hdl.handle.net/20.500.14394/6620">https://hdl.handle.net/20.500.14394/6620</a>

# Interplay Between Ion Transport, Applied Bias and Degradation under Illumination in Hybrid Perovskite p-i-n Devices

*Emily C. Smith,<sup>†,∇</sup> Christie L.C. Ellis,<sup>†,∇</sup> Hamza Javaid,<sup>†,∇</sup> Lawrence A. Renna,<sup>†,‡</sup> Yao Liu,<sup>§,○</sup>*

*Thomas P. Russell,<sup>§,⊥</sup> Monojit Bag,<sup>\*,†,||</sup> D. Venkataraman,<sup>\*,†</sup>*

<sup>†</sup>Department of Chemistry, University of Massachusetts Amherst, Amherst, Massachusetts

01003-9303, United States

<sup>§</sup>Department of Polymer Science and Engineering, University of Massachusetts Amherst,

Amherst, Massachusetts 01003-9303, United States

<sup>⊥</sup>Materials Science Division, Lawrence Berkeley National Laboratory, Berkeley, California

94720-1730, United States

## ABSTRACT

We studied ion transport in hybrid organic inorganic perovskite p-i-n devices as a function of applied bias under device operating conditions. Using electrochemical impedance spectroscopy (EIS) and equivalent circuit modeling, we elucidated various resistive and capacitive elements in the device. We show that ion migration is predictably influenced by a low applied forward bias, characterized by an increased capacitance at the hole transporting (HTM) and electron transporting material (ETM) interfaces, as well as through the bulk. However, unlike observations in n-i-p devices, we found that there is a capacitive discharge leading to possible ion redistribution in the bulk at high forward biases. Furthermore, we show that a chemical double layer capacitance buildup as a result of ion accumulation impacts the electronic properties of the device, likely by either inducing charge pinning or charge screening, depending on the direction of the ion induced field. Lastly, we extrapolate ion diffusion coefficients ( $\sim 10^{-7} \text{ cm}^2 \text{ s}^{-1}$ ) and ionic conductivities ( $\sim 10^{-7} \text{ S cm}^{-1}$ ) from the Warburg mass (ion) diffusion response, and show that, as the device degrades, there is an overall depletion of capacitive effects coupled with an increased ion mobility.

## INTRODUCTION

Hybrid organic-inorganic perovskites (HOIPs) have emerged as an important class of materials for a diverse array of applications, ranging from photovoltaics to memory storage.<sup>1-2</sup> An important feature of HOIPs is that they are mixed ionic-electronic conductors.<sup>1</sup> Unique behaviors emerge when electron transport is modulated by ion transport or when ion transport is modulated by electron transport. This interplay between ionic and electronic transport has been implicated as the cause of many important characteristics of HOIPs, such as instability to light and heat,<sup>3-4</sup>

hysteresis in current-voltage curves,<sup>5-7</sup> switchable photovoltaic effects,<sup>8</sup> thermoelectricity,<sup>9</sup> and increased power conversion efficiencies.<sup>10</sup> Thus, the interplay of electronic and ionic charge transport can significantly influence the functions of perovskites.<sup>11</sup> Understanding the relationship between these processes is, therefore, critical to developing new HOIPs with improved stability and superior device performance for energy harvesting as well as other electronic applications.

Electrochemical impedance spectroscopy (EIS)<sup>12-15</sup> is a powerful, non-destructive method to study charge and mass (ion) transport processes in mixed ionic-electronic conductors. Examining the current response over a range of AC voltage frequencies in EIS allows separation of processes that occur on different time scales, making it ideal for separating electronic and ionic processes in mixed conductors. EIS also provides information about charge and mass transport through the bulk as well as at grain boundaries and interfaces. EIS has been used to study HOIPs and these pioneering studies have shown the effect of device architecture, crystal size, and interface on the transport processes that occur in HOIPs.<sup>5, 16-33</sup> Yet, there is still no comprehensive understanding of ion transport in HOIPs *under device operating conditions*.

Here, we systematically investigate the effect of DC applied bias on ion transport in HOIP photovoltaic devices under illumination using EIS. We used a planar heterojunction device with a p-i-n architecture composed of methylammonium lead iodide (MAPbI<sub>3</sub>) perovskite with poly(3,4-ethylenedioxythiophene)-polystyrenesulfonate (PEDOT:PSS) as the primary hole transporting material (HTM) and [6,6]-phenyl-C<sub>61</sub>-butyric acid methyl ester (PCBM) as the electron transporting material (ETM). We also examine the impact of related factors such as photo-degradation of the device, interfacial characteristics, and fabrication method on ion transport under these conditions. We see evidence of ion accumulation at interfaces under a low

applied bias, consistent with our expectation and other experimental and theoretical studies.<sup>34-35</sup> However, at high forward biases, contrary to expectations, we found that there is a capacitive discharge leading to ion redistribution in the bulk.

## EXPERIMENTAL SECTION

**Methylammonium iodide synthesis.** Methylammonium iodide (MAI) was synthesized using a previously reported procedure.<sup>31</sup>

**MAPbI<sub>3</sub> Devices.** Photovoltaic devices were fabricated as previously reported<sup>31</sup> with minor deviations as follows: Poly(3,4-ethylenedioxythiophene)-polystyrenesulfonate (PEDOT:PSS) (Clevios PVP AI 4083) was filtered through a 0.45  $\mu\text{m}$  polytetrafluoroethylene (PTFE) filter (Wilkem Scientific), and was spin-coated onto ITO coated substrates ( $\sim 20 \Omega \text{ sq}^{-1}$ ) at 2500 rpm for 30 s. A solution of lead iodide, PbI<sub>2</sub>, in dry *N,N*-dimethylformamide (DMF) (400 mg mL<sup>-1</sup>) was filtered through a 0.45  $\mu\text{m}$  PTFE (Wilkem Scientific) filter and then heated to  $\sim 80^\circ\text{C}$ . This hot solution was spin coated at 6000 rpm onto a hot PEDOT:PSS-coated substrate ( $\sim 80^\circ\text{C}$ ) for 35 s. MAI was dissolved in isopropyl alcohol (40 mg mL<sup>-1</sup>) and was spin coated onto PbI<sub>2</sub>-coated substrates at 6000 rpm for 35 s at room temperature. The resultant MAPbI<sub>3</sub> samples were annealed ( $85^\circ\text{C}$ ) for 45 min. A solution of [6,6]-phenyl-C<sub>61</sub>-butyric acid methyl ester (PCBM) in chlorobenzene (20 mg mL<sup>-1</sup>) was spin coated atop the devices at 1000 rpm for 60 s followed by 2500 rpm for 10 s inside a N<sub>2</sub> filled glovebox ( $<1 \text{ ppm O}_2$ ,  $<1 \text{ ppm H}_2\text{O}$ ). A 15 nm thick calcium electrode was thermally deposited at chamber pressure of  $1 \times 10^{-6}$  mbar followed by 100 nm of aluminum electrode. The power conversion efficiency of the freshly-prepared device was measured to be  $\sim 11.5\%$ .

**Characterization.** Current density–voltage ( $J$ – $V$ ) curves were taken under an AM 1.5G solar simulator at  $100 \text{ mWcm}^{-2}$  light intensity inside a  $\text{N}_2$  filled glovebox.  $J$ – $V$  scans were obtained from  $-0.5 \text{ V}$  to  $1.5 \text{ V}$  at a scan rate of  $\sim 0.26 \text{ V s}^{-1}$ .

For EIS measurements, the AC amplitude was kept constant at  $20 \text{ mV}$  with varying DC applied voltages and the frequency ( $\omega$ ) was swept from  $1 \text{ MHz}$  to  $100 \text{ Hz}$ . EIS responses were fit from  $100 \text{ Hz}$  to  $0.2 \text{ MHz}$ . The device temperature was monitored by a thermoelectric heater/cooler at a constant current mode. The device temperature was measured under operating condition by a thermocouple attached to the heating/cooling stage.

For device degradation measurements, the devices were kept under continuous illumination, using a solar simulator, at open circuit condition for  $70$  except for  $15$  minutes during each  $J$ – $V$  and EIS measurements under done under dark for eight times. Device impedance was measured under dark conditions and under illumination at  $100 \text{ mWcm}^{-2}$  light intensity.

Powder X-ray diffraction (PXRD) measurements were made using a PANalytical X’Pert3 X-ray diffractometer with a Ni filter,  $1/2 \text{ in.}$  diverging slit, vertical goniometer, and X’Celerator detector. Measurements were taken from  $2\theta = 10^\circ$ – $50^\circ$  under  $\text{Cu K}\alpha$  ( $1.542 \text{ \AA}$ ).

## RESULTS AND DISCUSSION

EIS results are plotted by convention as Nyquist plots (Cole-Cole plots), with the real component of the impedance ( $Z'$ ) as the abscissa and the imaginary component ( $Z''$ ) as the ordinate. The data closest to the origin are associated with the higher frequency spectrum whereas the data farther from the origin are associated with the lower frequency spectrum. The Nyquist plots of our HOIP-based device under light at various PCEs and applied DC biases are shown in Figure S1. The Nyquist plots of HOIP-based p-i-n planar devices generally consist of

high frequency and low frequency components. Each component in the Nyquist plot can be modelled with a simple resistance-capacitance (RC) circuit. However, the low-frequency component requires a constant phase element (CPE)<sup>36</sup> with an exponent ( $\alpha \sim 0.5$ ) much lower than unity to fit the experimental results.

The observed large capacitance value under illumination has been attributed to charge accumulation at the interface,<sup>37</sup> a giant dielectric constant,<sup>38</sup> or ion transport.<sup>35, 39</sup> We observed a gradual degradation of MAPbI<sub>3</sub> to PbI<sub>2</sub> under heat and illumination (Figure S2),<sup>31</sup> indicating that the organic counterions (MA<sup>+</sup>) and/or iodide ions may diffuse towards the electrode. In previous studies we have shown a dependence of the low-frequency component on the size of the organic counterion.<sup>31</sup> We therefore surmised that ion accumulation at the electrode interfaces building up a double layer may be the origin of this large capacitance value. Our hypothesis is consistent with similar observations in EIS measurements of mixed ionic-electronic conductors.<sup>12, 15</sup> Therefore, we added a Warburg constant phase element to the equivalent circuit model for the low frequency component to account for ion transport.<sup>40</sup> To verify the Warburg impedance in our devices, the imaginary ( $|Z''|$ ) and real ( $|Z'|$ ) components of  $Z(\omega)$  were plotted as a function of  $\omega^{-1/2}$ , as shown in Figure S3.<sup>41</sup> The extrapolation of  $|Z''|$  to  $\omega^{-1/2} = 0$ , intersecting the ordinate at zero, clearly indicates the presence of a Warburg diffusional process.

The complete equivalent circuit model is shown in Figure 1b. We have used this model in our previous studies,<sup>31, 42</sup> where we also analyzed several equivalent circuit models and showed that the model depicted in Figure 1b is robust for our devices.<sup>42</sup> The Warburg model for analyzing EIS data of HOIPs has also been independently validated by Fan and co-workers.<sup>33</sup> In the circuit model, the high frequency component in the Nyquist plot is represented by a combination of recombination/transport resistance ( $R_{tr}$ ) and a bulk capacitance ( $C_{bulk}$ ). Warburg diffusion is

always associated with interfacial charge transfer resistance ( $R_{ct}$ ) arising from imperfect electrode contacts and a double layer capacitance ( $C_{dl}$ ) due to ion accumulation. Electronic resistance ( $R_{electr}$ ) in parallel to the bulk capacitance ( $C_{bulk}$ ) captures charge transport/recombination originating from the electronic charge carriers (free electrons and holes) that are not coupled to ion diffusion/accumulation at the interface.  $R_S$  is the series resistance of the device.<sup>13</sup> Using Z-View 3.4c (Scribner Associates Inc.), we fit the experimental EIS data to this model using least-squares refinement. The circuit components and  $\chi^2$  (goodness-of-fit) for two-step devices are given in Figures 3-4 and Figures S4-5.

We used this equivalent circuit model to analyze EIS spectra to characterize ion diffusion in planar MAPbI<sub>3</sub> devices as a function of applied bias and device degradation. We calculated ion diffusion coefficients ( $D$ ) from Warburg time constants ( $T_W$ ) and ionic conductivities ( $\sigma_{ion}$ ) from Warburg resistance ( $W_R$ ). We also analyzed the trends in these values and in the capacitive and resistive elements to comprehensively understand ion migration in HOIP devices.

Our results show that the devices have three distinct response regions: in the low (0 mV - 400 mV), medium (400 mV - 600 mV), and high (>600 mV) levels of  $V_{app}$ . We will henceforth refer to these bias ranges as low, medium, and high  $V_{app}$ . We found that the trends in the circuit elements at low and high biases are opposite. An inflection point is seen at medium biases and the bias at inflection point closely corresponds to the voltage at maximum power point of the devices ( $V_{mpp}$ ). We attribute these trends to ion migration through the bulk and ion accumulation at the interfaces, which is initiated by illumination, and affects the electronic properties of the devices. The degradation of the device over time decreases the ability of ions to respond to applied bias and illumination.

We compared our results to a model introduced by Cameron, Peter and coworkers as the basis for analyzing our results.<sup>32</sup> They suggested that, in a n-i-p HOIP device under illumination, a large photovoltage ( $V_p$ ) of  $\sim 0.5$  V is introduced by photocarriers in a direction that opposes the original built-in field ( $V_{bi}$ ), effectively discharging ions that have accumulated as a response to the  $V_{bi}$  under dark conditions.<sup>32</sup> In our experiments, we apply a forward bias to HOIP devices under illumination. Therefore, we are applying a field that adds to the existing  $V_p$ . This added field induces further redistribution of ions throughout the bulk. It would follow from the Cameron and Peter model that as we increase the applied bias ( $V_{app}$ ), we will eventually reach a point where the sum of  $V_p$  and  $V_{app}$  will become equal to  $V_{bi}$ . At this point, there will be no net directional driving force for the ion to migrate. We designate this net driving force as  $V_{net}$ . Increasing  $V_{app}$  beyond this point will result in a reversal of the driving force leading to ion accumulation at the opposite electrodes of the device. As the ions start to accumulate, there is a build-up of a Coulombic potential. At the inflection point, Coulombic potential is higher than the applied potential, which leads to the redistribution of ions in the bulk, effectively discharging the double layer capacitance (Figure 2). This hypothesis is also consistent with a model proposed by Snaith, Lin, Johnston and coworkers, where they invoked ion accumulation at the HOIP-electrode interfaces to explain why perovskite solar cells can function efficiently even without an ETM.<sup>43</sup> Alternatively, it is also possible that device may start to degrade under these conditions, which may result in the redistribution of ions thus reducing the double layer capacitance.

**Bias-dependent analysis.** The EIS results for the device under illumination at  $V_{app} = 0$  V is shown in Figure 1a. Powder X-ray diffraction of the MAPbI<sub>3</sub> is shown in Figure S2 and indicates a small amount of PbI<sub>2</sub> is leftover in the film.  $J$ - $V$  curves for our p-i-n devices typically show a small degree of hysteresis (Figure S6). From the equivalent circuit model, we determined the

bulk capacitance ( $C_{bulk}$ ) to be  $\sim 3$  nF and the interfacial double layer capacitance ( $C_{dl}$ ) to be  $\sim 0.3$   $\mu$ F respectively, at  $V_{app} = 0$  V (Figure 3a-b). Since  $C_{dl}$  is obtained from the low-frequency component of the impedance spectra, we surmise that this capacitance is associated with the ion build-up at the interfaces. However, this ion build-up can also pin electron charges at the interface, and thus can contribute to the absolute values of the capacitance. This hypothesis has been successfully used to explain the origin of  $J$ - $V$  hysteresis in HOIPs.<sup>35, 44-46</sup> We found that at low  $V_{app}$ , there is minimal change to either  $C_{bulk}$  or  $C_{dl}$  in devices with a certain degree of active layer degradation. In the device with the highest power conversion efficiency (PCE) of 11.45%, we found that both the  $C_{dl}$  and  $C_{bulk}$  increase as a function of  $V_{app}$  in the low range.

At medium  $V_{app}$ , we found that there is a steady increase in  $C_{bulk}$  and  $C_{dl}$ , indicating that ions have begun accumulating at opposite interfaces (cations at the ETM and anions at the HTM) creating a new double layer, consistent with our hypothesis. If we assume that there is a photoinduced voltage,  $V_p$ , in our device that opposes the  $V_{bi}$ , then the  $V_p$  can be estimated using the point where ion accumulation begins to flip direction ( $V_{app} = 0.4$  V). This would be where the additive  $V_p$  and  $V_{app}$  are able to overcome the intrinsic  $V_{bi}$ . The  $V_{oc}$  of this device at all PCEs (besides the pristine device) is  $\sim 0.9$  V (Table S1). From this, we can estimate that the  $V_p$  in our p-i-n device is  $\sim 0.5$  V. This value is similar to  $V_p$  that was calculated by Cameron, Peter, and coworkers for an n-i-p device using transient photovoltage measurements. We therefore surmise that the nature of the  $V_p$  is not largely impacted by interfacial characteristics. The measured  $V_{oc}$  for the highest performing device is slightly lower (0.81 V) which may explain the increase in  $C_{dl}$  at lower  $V_{app}$  for that device.

At medium  $V_{app}$ ,  $C_{dl}$  increases by  $\sim 900\%$ , with a maximum value at  $V_{app} = 0.6$  V, as opposed to the modest increase in  $C_{bulk}$  (42% increase), with a maximum value at  $V_{app} = 0.7$  V. As we

continue to high  $V_{app}$ , we see a reversal in trends in both bulk and double-layer capacitances. We attribute this trend to the increase in effective  $V_{bi}$  at the inflection point caused by the increased Coulombic potential due to ion accumulation at the interfaces. At even higher applied biases, there is a discharge of the double layer capacitance. It is important to note that this decrease does not appear to approach 0  $\mu\text{F}$ , indicating that despite the ionic discharge, there is still a measurable double layer. It is also important to note that the inflection point, following which  $C_{dl}$  begins to decrease, occurs at a lower voltage than the  $V_{oc}$  where one might expect to see this inflection. This may be due to charge accumulation, which can alter the charge recombination kinetics, thus altering the  $V_{oc}$ .<sup>32</sup> We note that this value is consistently closer to the  $V_{mpp}$  of the device ( $\sim 0.7$  V) observed in  $J$ - $V$  curves than to the  $V_{oc}$ .

We then prepared a HOIP device using an alternate method (Note S1) which has a different  $V_{mpp}$  and similar EIS trends were observed with an inflection point that corresponded more closely to the  $V_{mpp}$  than to the  $V_{oc}$  of the device. These observations indicate that there are large capacitive effects when the device is at the highest power output at  $V_{mpp}$ . Snaith and coworkers used a numerical drift-diffusion model to simulate hysteresis in perovskite solar cells.<sup>35</sup> This model predicts that when ion accumulation occurs in the direction of the  $V_{bi}$ , effective charge screening occurs which leads to a higher photocarrier concentrations and fewer recombination events.<sup>35</sup> From this analysis, we conclude that the highest power output in our devices is at the point where there is maximum ion accumulation inducing a field in the direction of the  $V_{bi}$ . We note that this bell-shaped curve was not observed by Pauporté and coworkers in HOIP devices containing mesoporous  $\text{TiO}_2$  as the ETM, indicating that the nature of the ETM and HTM may play a large role in ion accumulation behavior.<sup>47</sup> Varying  $J$ - $V$  hysteresis responses across devices

with p-i-n versus n-i-p architecture is well documented, further underscoring the need to consider device architecture when analyzing ion transport.<sup>45</sup>

We observe that the maximum value of  $C_{dl}$  appears at lower  $V_{app}$  than the  $C_{bulk}$  maximum (Figure S7). We expect that the bulk capacitance should be impacted by changes in ion distribution within the bulk and should not vary with the double layer formation. Therefore,  $C_{bulk}$  should reach a maximum at a  $V_{app}$  after the double layer has begun to discharge. Indeed, we see that the  $C_{bulk}$  maximum is broad and offset slightly from  $C_{dl}$  towards higher  $V_{app}$  indicating that the discharge of  $C_{dl}$  is accompanied by a charge redistribution within the bulk.

To further confirm that this capacitive response is predominately due to ion accumulation at the interfaces, we fabricated devices with a cationic, anionic, or zwitterionic-based HTM and studied their EIS response as a function of bias. We fabricated these devices in a one-step method using a previously described procedure.<sup>42</sup> Changing the HTM to a cationic poly(benzothiadiazole vinylene-alt-2,5-bis(5-(N,N,N-trimethylammonium bromide)hexyloxy)-1,4-phenylenevinylene), or anionic poly(benzothiadiazole vinylene-alt-2,5-bis(4-sodium sulfonate)butoxy)-1,4-phenylenevinylene) yields trends in capacitance similar to those in the PEDOT:PSS devices, but with a shifted inflection point to higher  $V_{app}$  for the anionic HTM (Figure S8). We expect that  $MA^+$  ions will accumulate at the HTM at lower  $V_{app}$  and, thus, we expect the anionic HTM to be capable of counter ion exchange with  $MA^+$  ions, shifting the point of inflection to higher biases. In our prior studies, we have established that the anionic and cationic HTM do not act as adsorbing interfaces and the ions move to and from the boundary through ion exchange mechanisms. These devices also show low hysteresis in  $J-V$  curves regardless of the scan rates. On the other hand, the zwitterionic polymer (poly(benzothiadiazolevinylene-alt-2,5-bis((N-(3-sulfonato-1-propyl)-N,N-

dimethylammonium)hexyloxy)-1,4-phenylenevinylene), showed significant  $J$ - $V$  hysteresis as a result of a dipole-induced interaction between the freely rotating zwitterionic moieties of the HTM and accumulating interfacial ions. We consider this interface to be adsorbing for ions, which confirmed the interpretation of the low frequency features in the EIS response. We observed overall capacitive trends that are similar to the other HTMs with minor differences. The onset of  $C_{dl}$  occurs at lower  $V_{app}$  and there is a broad inflection point in the double layer capacitance-voltage curve which extends into high  $V_{app}$ . These observations are consistent with an interface that has strong adsorbing interactions with both  $MA^+$  and  $I^-$ .<sup>42</sup> The shift in bias-dependent capacitive trends with the changing of HTMs is a clear indication that we are capturing ion accumulation at this interface, strongly suggesting that organic cation is possibly mobile in this system.

Interestingly, such bell-shaped capacitance-voltage curves have been observed in electrochemical studies of room temperature ionic liquids (RTILs), where the maxima of capacitance corresponds to the potential of zero charge for the electrode.<sup>48-49</sup> These systems have been modeled using mean field theory with a value  $\gamma$  representing the ratio of the average ionic concentration to the maximum possible local concentration.<sup>50</sup> Thus, ion size, mobility, and packing parameters at the double layer play a crucial role in the capacitance-voltage curves of these systems. In the case of RTILs, the inflection point is attributed to a stage where all voids in the double layer are filled and counter ions begin to line the electrode. Surpassing this stage leads to a decrease in capacitance.<sup>49</sup> We concluded that this is not likely a scenario for our system, as we see an increase in ion mobility and  $C_{bulk}$  at higher  $V_{app}$ , indicating a loosely packed double layer capable of redistributing ions into the bulk. Nevertheless, the similarities between

capacitance-voltage measurements of RTILs and HOIPs underscores the high ionic mobility and the crucial role that ion migration plays in the operation of HOIPs.

Generalized Warburg diffusion  $W_S$  is described by the equation:

$$W_S = A_w \frac{\tanh(j\omega T_w)^P}{(j\omega T_w)^P}$$

where  $T_w$  is the Warburg time constant,  $A_w$  is the Warburg impedance and the exponent  $P$  is  $\sim 0.5$  for finite-length Warburg diffusion.<sup>51</sup> State-of-the-art first-principle calculations indicate that iodide migration would occur on timescales  $< \mu\text{s}$ ,<sup>52</sup> much lower than the ms timescale where we observe the Warburg response; thus, we assume that the iodide migration response overlaps the electronic response in the high frequency (first) semicircle. Additionally, a change in Warburg response as a function of organic cation substitution coupled with the observed activation energy barrier suggests that the Warburg diffusion may arise from  $\text{MA}^+$  migration.<sup>31</sup> However, we do not rule out other possibilities for the migrating ion under the device operating conditions. At low applied bias, we see evidence of a Warburg response in the low frequency region indicative of semi-infinite mass diffusion characterized by a linear impedance response approximately  $45^\circ$  from the real axis. As  $V_{app}$  is increased the linear portion of the Nyquist plot begins to curve back toward the real axis, which is characteristic of mass diffusion to either a reactive or adsorbing boundary. The characteristics of interfacial Warburg responses are explained in detail in a previous work.<sup>42</sup> Since we do not anticipate an electrochemical reaction to be occurring between ions and the interfaces, we propose that at higher  $V_{app}$  the Warburg curvature back into the real axis indicates an adsorbing boundary. Due to the relatively reduced hysteresis in planar p-i-n devices we suspect that, while the boundary may be slightly adsorbing at prolonged medium biases, we see from ion mobility calculations that it does not significantly affect bulk ion mobility under operating conditions. This observation does not rule out deep ionic trap states at

interfaces leading to degradation of the device, nor does it account for any possible iodide migration to the PEDOT:PSS layer.

It is clear that ions become more mobile under higher biases, as we see a decrease in Warburg impedance ( $A_w \sim 3000 \Omega$  at  $V_{app} = 0 \text{ V}$  to  $A_w \sim 200 \Omega$  at  $V_{app} = 0.6$ ) and Warburg time constant ( $T_w \sim 7 \text{ ms}$  at  $V_{app} = 0 \text{ V}$  and  $\sim 1 \text{ ms}$  at  $V_{app} = 0.6 \text{ V}$ ). The increase in  $C_{dl}$  in the intermediate range of  $V_{app}$  suggests that while the ions may be more mobile in the bulk, there is an increase of ion buildup at interfaces. Additionally, as the number of defect sites increase throughout the bulk, ions are expected to move more freely through these defects. We validate this hypothesis using the comparison of  $A_w$  to PCEs where we see a decreasing Warburg impedance as a function of device degradation (Figure 4a, 4b) discussed in detail in the ensuing section.

From  $T_w$  we can estimate ion diffusion coefficients ( $D$ ) for the mobile ion using the equation:

$$D = \frac{L_D^2}{T_w}$$

Where  $L_D \approx 300 \text{ nm}$ , corresponding to the film thickness measured by profilometry. We calculated  $D$  values on the order of  $10^{-7} \text{ cm}^2 \text{ s}^{-1}$  (Figure 5 and Table S2) and found that the effective diffusion coefficients remain constant at lower biases, and steadily increase after  $V_{app} \approx 0.5 \text{ V}$ , as would be expected as ions are biased in the opposite direction. Also, we also did not observe any decrease in the  $D$  values as  $C_{dl}$  reaches its maxima.

We can estimate ionic conductivity ( $\sigma_{ion}$ ) from the equation:

$$\sigma_{ion} = \frac{d}{\alpha \times A_w}$$

Where  $\alpha = 0.06 \text{ cm}^2$  and is the electrode area. We calculate  $\sigma_{ion} \sim 10^{-7} \text{ S cm}^{-1}$  for EIS scans at low  $V_{app}$  and see that  $\sigma_{ion}$  increases two orders of magnitude to  $\sim 10^{-5} \text{ S cm}^{-1}$  as higher biases are applied, as anticipated from the increasing  $D$  at higher  $V_{app}$  (Figure 5). Overall, we conclude that

despite the buildup of an ionic double layer at the interface, ions through the bulk become significantly more mobile in response to higher biases, likely due to increased defect sites.

The  $R_{tr}$  term, indicating electronic charge transport and recombination in the bulk material, follows an opposite trend to that of capacitance, reaching a minimum in the medium  $V_{app}$  range (Figure S5).  $R_{tr}$  values on the order of  $10^4 \Omega$  are reported at low  $V_{app}$ , decreasing to  $10^3 \Omega$  at  $V_{app} = 0.6$  V. The results at low  $V_{app}$  are consistent charge pinning that arises from electronic charge carriers stabilizing accumulated ions, effectively creating a double layer of ions and pinned charges.<sup>35</sup> In the medium region of  $V_{app}$ , ions begin accumulating at interfaces favorable to charge screening and thus we anticipate a decreased  $R_{tr}$  term.<sup>35</sup> In conjunction with this hypothesis, at the point of highest capacitance we see a minimum in  $R_{tr}$  indicating favorable charge screening close to the  $V_{mpp}$  of the device. As the double layer capacitance discharges at higher biases, we see an increase again in  $R_{tr}$ .

Decreasing carrier lifetimes (estimated using the minima of the first semicircle) in the medium range of  $V_{app}$  suggests that the increased mobility of ions induces lower carrier lifetimes; however, our estimated lifetimes are on the order of  $10^{-5}$  s, orders of magnitude larger than commonly reported values ( $\sim 10^{-6}$  s -  $10^{-9}$  s).<sup>32</sup> Therefore, this estimation is likely not a true representation of the electronic carrier lifetime. We believe that this may be another indication that iodide migration may be captured in the first semicircle, rendering it both electronic and ionic in nature. Additionally, at high forward  $V_{app}$  we see increased minority carrier recombination, which will influence these estimated values.

Similar bias dependent trends were observed in a device fabricated using a one-step method, with variations in onset and magnitude of the observed responses. We have detailed the fabrication method and bias response comparisons in Note S1.

**Device Degradation.** We performed bias-dependent EIS on a HOIP device as it aged, monitoring PCE as a measure device degradation. The device degraded from an initial PCE of 11.5% to a final measured PCE of 4.6%. We found similar trends in EIS parameters throughout the aging process, including the three distinct regimes of behavior: low, middle, and high  $V_{app}$ . However, differences in initial values and shifts in inflection point onset were observed.

The initial values of both  $C_{bulk}$  and  $C_{dl}$  generally decrease with decreasing PCE. Both capacitances exhibit the same bell-shaped capacitance-voltage curves observed in the fresh device, but the capacitance maxima decrease in magnitude and shifts to a higher bias for both  $C_{bulk}$  and  $C_{dl}$  as the device degrades below 8.8%. Thus, a higher bias is required to move the ions to the interfaces and also discharge the double layer once  $V_{app} > V_{bi} + V_p$ . This indicates an increase in  $V_{bi}$  as the device degrades. The peak in  $C_{dl}$  is sharper at all PCEs than the peak in  $C_{bulk}$ , indicating that regardless of degradation, the ions at the double layer respond more quickly than those throughout the bulk. Additionally, the height of the peak in relation to the initial values decreases for both  $C_{bulk}$  and  $C_{dl}$ . At the lowest PCE of 4.6%, the peak for  $C_{bulk}$  is barely discernable from the initial and final steady state values. This can be justified by considering both defect sites enhancing ion mobility at interfaces and an increasing number of ionic trap states as the device degrades.

Initial values of  $T_w$ , the Warburg time constant, decrease as the device degrades. This trend indicates that ions are moving faster in the degraded devices, likely due to the increase in defect sites or grain boundaries through which ions can move. The decrease in capacitance coupled with faster ionic motion indicates that while the ions can move faster by taking advantage of vacancy defects, the total number of mobile ions has decreased as larger numbers of ions become trapped in grain boundaries or at interfaces. The  $T_w$  at all PCEs drops near the  $V_{mpp}$ , and this

decrease occurs at higher biases as the device degrades. However, the  $T_w$  at each PCE is more similar in the high bias regime than in the low or mid biases. This increase in conductance of ions is supported by the Warburg resistance,  $A_w$ , values, which decrease as the device degrades.  $A_w$  also shows a similar decrease to  $T_w$  around  $V_{mpp}$ , where values at each PCE become much closer at high bias. Warburg exponent  $P$  values for all PCEs show a slight increase throughout the degradation process, indicating that the interfacial boundary becomes more reflective (less adsorbing) as the HOIP layer degrades. This is consistent with the decreased  $C_{dl}$  observed with aging. The value of  $R_{tr}$  shows a relatively steady initial value at low biases at all PCEs, which decreases as the device degrades. At medium bias  $R_{tr}$  decreases and reaches a minimum before increasing again at high bias.

At each PCE, we generated a Mott-Schottky plot by using the inverse geometric capacitance-voltage relationship (Figure 6a). The slope of the linear response is a measure of p-doping density of electrical defects and the abscissa-intercept gives information about the flat band potential ( $V_{fb}$ ).<sup>53</sup> We see minimal change in device defect density across degraded devices at higher PCEs as the slope of the linear portions remain relatively constant. As the device degrades below a PCE of 7%, the slope increases, indicating an increase in p-type defects as a function of degradation. In devices with high PCEs, the  $V_{fb}$  increases as the device degrades from 11.45% to 7.4% (Figure 6b). These two observations are consistent with observations by Bisquert, Yang and co-workers,<sup>53</sup> and indicate that the properties of the bulk remain relatively unchanged as a function of bias while the device is above 7% PCE but the electronic properties of the PCBM cathode interface are influenced significantly in these high efficiency devices. This is consistent with an increase in  $V_{bi}$  as the device degrades. A large  $V_{fb}$  in inefficient devices suggests that

there is less beneficial ion accumulation at interfaces, corroborated by the decreased capacitance for low PCE devices as well as the increased defect density.

## CONCLUSION

In conclusion, we have determined that ions in HOIP photovoltaic devices respond to bias and illumination in a predictable manner by diffusing through the bulk and accumulating at specific interfaces. When the sample is illuminated, a photovoltage is induced in the opposite direction of the  $V_{bi}$ , decreasing  $V_{net}$ , and causing the ions to migrate towards the opposite interfaces. When low forward biases are applied, the ions begin to diffuse steadily towards the opposite interfaces, with the magnitude of  $V_{net}$  shrinking, and eventually reversing sign and increasing in the opposite direction (aligned with  $V_{bi}$ ). The cations now begin to accumulate near the ETM and the anions near the HTM until the accumulation reaches a maximum, which corresponds to the inflection point in bias trends near the  $V_{mpp}$ . At this point, ion accumulation creates a strong field in the same direction as  $V_{bi}$ , giving the highest observed capacitance values both across the device ( $C_{bulk}$ ) and in the double layer at the interfaces ( $C_{dl}$ ). Anions at the HTM stabilize the transport of positively charged holes to the HTM and destabilize electrons at this interface, decreasing recombination and increasing charge extraction. The reverse holds true for cation accumulation at the ETM, resulting in minimum charge transport resistance ( $R_{tr}$ ). At high biases, ion accumulation induces an increase in  $V_{bi}$  causing ions to redistribute back into the film, leading to a decrease in capacitance and an increase in  $R_{tr}$ .

## FIGURES

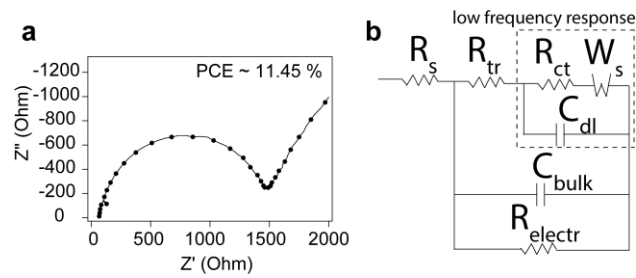


**Figure 1.** (a) Example of an EIS response plotted in complex space for the 11.5% PCE device. The high frequency (left) portion of the plot shows a semicircle attributed to fast ionic/electronic conduction processes and the low frequency portion (right) side shows a linear portion  $\sim 45^\circ$  with respect to the abscissa attributed to ionic mass diffusion. (b) The equivalent circuit model used to fit all data. Details of each element are described in the text.

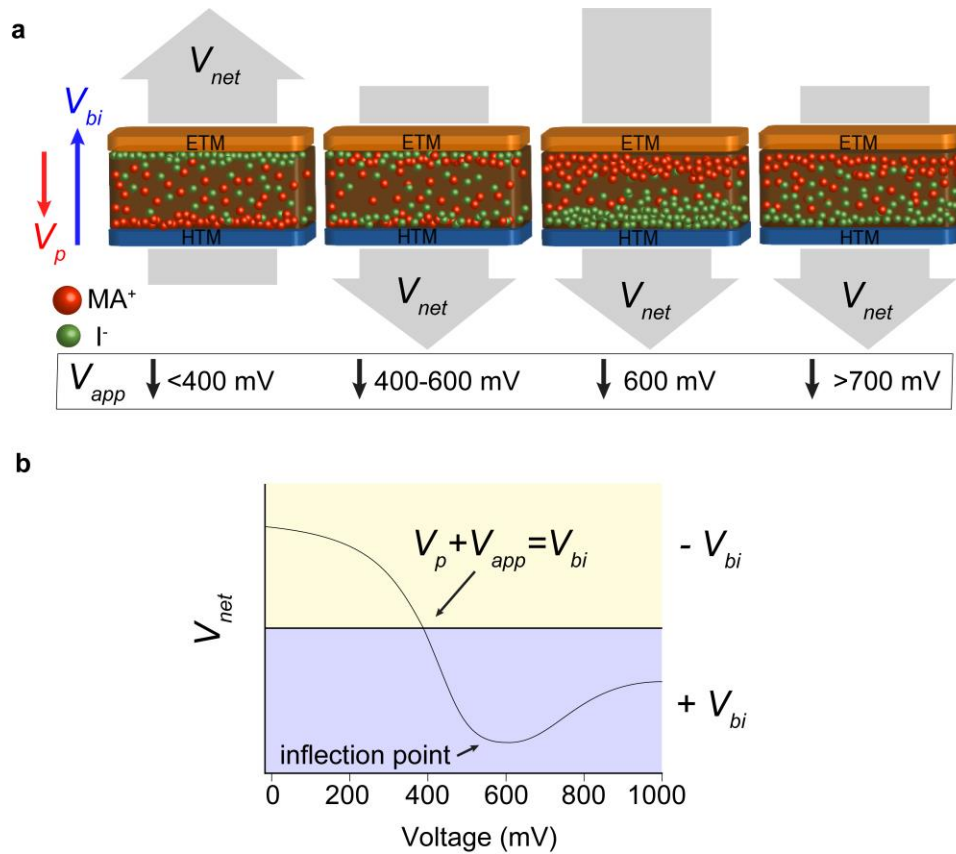


**Figure 2.** (a) Schematic of the response in a HOIP device under varying applied bias ( $V_{app}$ ). The photo-induced voltage ( $V_p$ ) and built in voltage ( $V_{bi}$ ) remain constant at low  $V_{app}$ , thus,  $V_{net}$  must fluctuate to maintain equilibrium.  $V_{net}$  flips to oppose the  $V_{app}$  at 400 mV, when the capacitance-voltage relationship indicates ion accumulation beginning to switch direction.  $V_{net}$  continues to increase to compensate for increasing  $V_{app}$  until the inflection point ( $\sim 600$  mV) when ion accumulation alters the  $V_{bi}$ , inducing ion discharge at higher biases. (b) A qualitative representation of the magnitude shifts in  $V_{net}$  as a function of  $V_{app}$ . The point at 400 mV where  $V_{net}$  is neither opposing the  $V_{bi}$  ( $-V_{bi}$ ) nor in the direction of  $V_{bi}$  ( $+V_{bi}$ ) occurs when the sum of  $V_p$  and  $V_{app}$  equals the  $V_{bi}$ . Increasing the bias further requires  $V_{net}$  to change direction to compensate the increasing electric field.

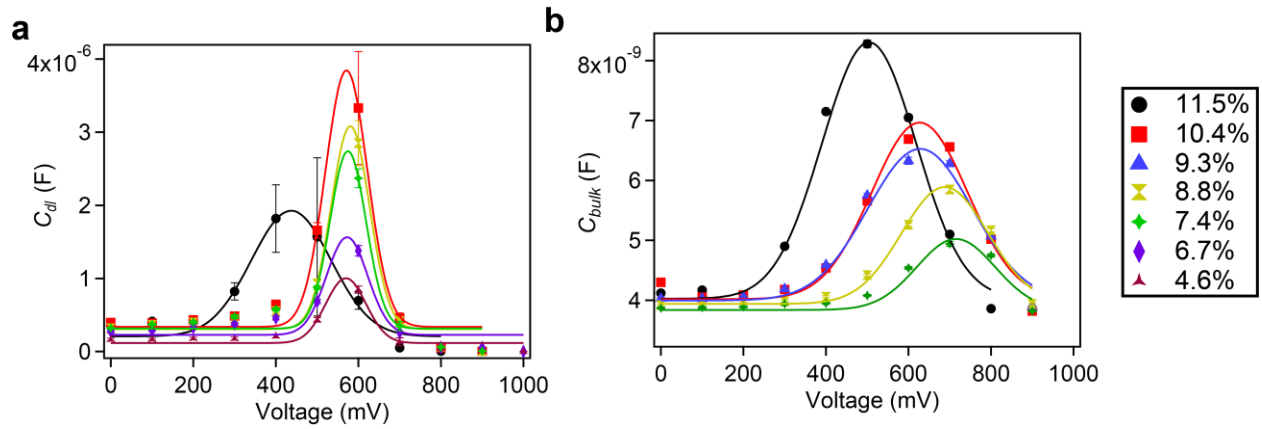


**Figure 3.** Values for EIS equivalent fit circuit elements plotted as a function of DC bias at different device power conversion efficiencies. The legend for all PCEs can be found top right (a) Double layer capacitance ( $C_{dl}$ ) represents the low frequency capacitive response at the ETM/HTM interface and is seen to increase as ions are biased initially, then decrease again at higher biases. As the device degrades, a shift in inflection point and a decrease of maximum capacitance indicates more deep ion trap states. (b) Bulk capacitance ( $C_{bulk}$ ) models high frequency and bulk capacitance arising from fast ionic/electronic charge distribution in the bulk and follows the same trend as (a). Data from (a) &(b) are fit with Gaussian functions. Error bars for fits are shown. If error bars are not seen it is because the error was less than 5% and the bars have been obscured by the data point.

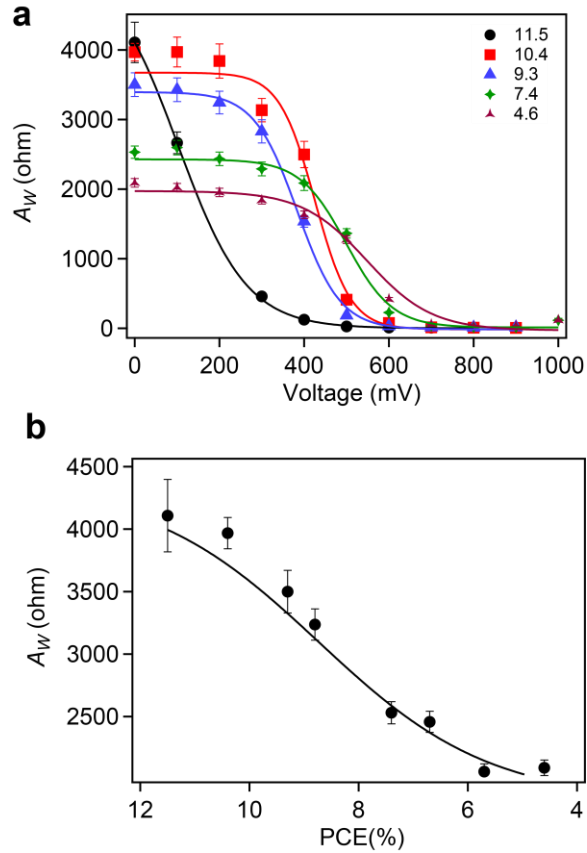


**Figure 4.** (a) Warburg resistance ( $A_w$ ) as a function of bias at different device PCEs. As the capacitive double layer begins to build (400 mV), resistance to mass diffusion begins to decrease as ions are biased in the direction of  $V_{bi}$ . (b) Warburg resistance ( $A_w$ ) for each PCE scan at  $V_{app} = 0$  V as a function of degradation. Resistance to mass transport decreases steadily as the device degrades, indicating ions become more mobile with increased defect sites. Data from (a) & (b) are fit with Sigmoid functions. Error bars for fits are shown. If error bars are not seen it is because the error was less than 5% and the bars have been obscured by the data point.

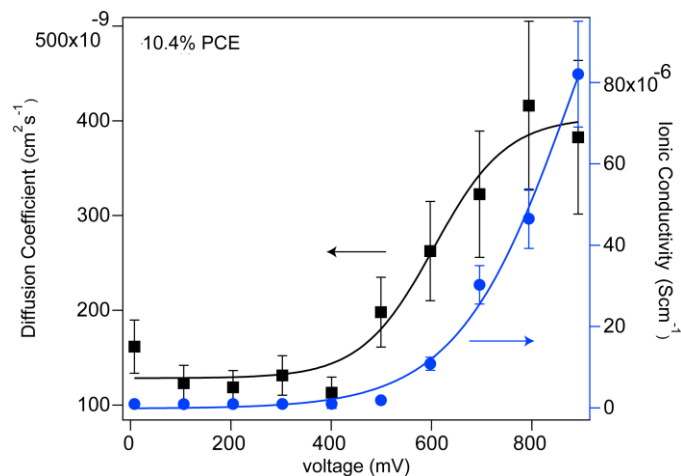


**Figure 5.** Ionic diffusion coefficients (black, left) calculated from the Warburg time constant, and ionic conductivity (blue, right) calculated from the Warburg resistance for the device at 10.5% efficiency. Data from diffusion coefficients is fit with a Sigmoid function and error is taken from the average error for  $T_w$  fits, and the ionic conductivity is fit as a Gaussian and error is taken from the average  $A_w$  fits.

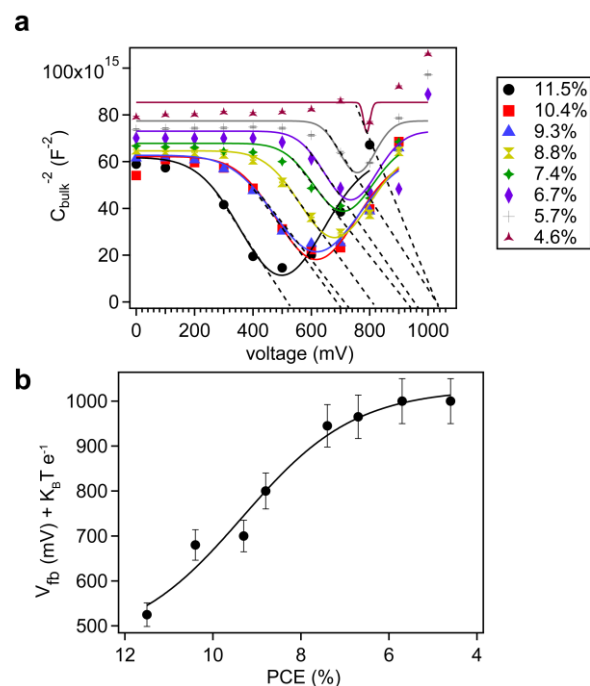


**Figure 6.** (a) Mott-Schottky plot taken from inverse square of the bulk capacitance ( $C_{bulk}$ ). The negative slope gives us insight into the p-doping density of the HOIP, and the linear region that intersects the abscissa axis gives us information about the flat band potential ( $V_{fb}$ , dotted line). (b) Flat band potential extrapolated from (a) as a function of degradation where  $K_B$  is Boltzmann constant,  $T$  is temperature and  $e$  is electronic charge. There is a rapid increase in  $V_{fb}$  at higher PCEs that begins to equilibrate close to 1 V at PCEs below 7%. Data from (a) is fit to a Gaussian and data from (b) is fit with a Sigmoid function. Error for (b) is taken to be 5%. Error bars from (a) are not seen because the error was less than 5% and the bars have been obscured by the data point.

## ASSOCIATED CONTENT

### Supporting Information.

Nyquist plots for two-step devices at different PCEs and biases, Nyquist plots for one-step devices at different biases, X-ray diffraction of MAPbI<sub>3</sub> under heat and illumination, X-ray diffraction of two-step method, evidence of Warburg diffusion, EIS fit values for one-step and two-step preparation methods, ionic conductivity ( $\sigma_{\text{ion}}$ ) values for one-step method, diffusion coefficients for both one and two-step method, comparison of geometric and double layer capacitance for two-step method, comparison of one-step and two-step methods, *J-V* characteristics of one-step and two-step method, double layer capacitance for devices with different HTMs, equivalent fit trends for the one-step method ([PDF](#)). A complete dataset of circuit parameters obtained by fitting the impedance spectra to the circuit model for device studied is freely available at DOI: <https://doi.org/10.7275/R52805TR>

## AUTHOR INFORMATION

### Corresponding Author

\*(D. Venkataraman) Email: [dv@umass.edu](mailto:dv@umass.edu)

\*(Monojit Bag) Email: [mbagfph@iitr.ac.in](mailto:mbagfph@iitr.ac.in)

### Present Addresses

<sup>‡</sup>Department of Chemistry, University of California Irvine, Irvine, California 92697-2025, United States

<sup>○</sup>Beijing Advanced Innovation Center for Soft Matter Science and Engineering, Beijing University of Chemical Technology, Beijing, 100029, China

<sup>‖</sup>Department of Physics, Indian Institute of Technology Roorkee, Roorkee, Uttarakhand 247667, India

### Author Contributions

<sup>▽</sup> Emily C. Smith, Christie L. C. Ellis and Hamza Javaid contributed equally.

## Notes

The authors declare no competing financial interests.

## ACKNOWLEDGMENT

This work was partially supported as part of Polymer-Based Materials for Harvesting Solar Energy (PHaSE), an Energy Frontier Research Center funded by the U.S. Department of Energy, Office of Science, Basic Energy Sciences under Award No. DE- SC0001087. Y.L. and T.P.R. acknowledge support by the Office of Naval Research, Materials Division, under contract N00014-17-1-2241. We thank the Laboratory for Electronic Materials and Devices of the Institute for Applied Life Sciences at the University of Massachusetts, Amherst. We also thank Dr. Zachariah A. Page and Prof. Todd Emrick for providing the ionic HTMs and ETM.

## ABBREVIATIONS

$V_{app}$ , applied bias;  $V_{net}$ , net Coulombic potential;  $V_{bi}$ , built in bias;  $V_{oc}$ , open circuit voltage;  $V_p$ , photoinduced voltage;  $V_{mpp}$ , voltage at maximum power point;  $R_s$ , series resistance;  $R_{tr}$ , charge transport resistance;  $R_{ct}$ , charge transfer resistance;  $R_{elec}$ , electronic transport resistance;  $C_{bulk}$ , bulk capacitance;  $C_{dl}$ , double layer capacitance;  $A_w$ , Warburg impedance;  $T_w$ , Warburg time constant;  $D$ , diffusion coefficient;  $d$ , film thickness;  $\sigma_{ion}$ , ionic conductivity;  $L_D$ , diffusion layer thickness,  $MA^+$ , methyl ammonium;  $I^-$ , iodide; HTM, hole transporting material; ETM, electron transporting material; EIS, electrochemical impedance spectroscopy

## REFERENCES

- (1) Tress, W. Metal Halide Perovskites as Mixed Electronic–Ionic Conductors: Challenges and Opportunities—from Hysteresis to Memristivity. *J. Phys. Chem. Lett.* **2017**, *8*, 3106-3114.
- (2) Ono, L. K.; Juarez-Perez, E. J.; Qi, Y. Progress on Perovskite Materials and Solar Cells with Mixed Cations and Halide Anions. *ACS App. Mater. Inter.* **2017**, *9*, 30197-30246.
- (3) Bryant, D.; Aristidou, N.; Pont, S.; Sanchez-Molina, I.; Chotchunangatchaval, T.; Wheeler, S.; Durrant, J. R.; Haque, S. A. Light and Oxygen Induced Degradation Limits the Operational Stability of Methylammonium Lead Triiodide Perovskite Solar Cells. *Energy Environ. Sci.* **2016**, *9*, 1655-1660.
- (4) Yuan, H. F.; Debroye, E.; Janssen, K.; Naiki, H.; Steuwe, C.; Lu, G.; Moris, M.; Orgiu, E.; Uji-i, H.; De Schryver, F. et al. Degradation of Methylammonium Lead Iodide Perovskite Structures through Light and Electron Beam Driven Ion Migration. *J. Phys. Chem. Lett.* **2016**, *7*, 561-566.
- (5) Richardson, G.; O’Kane, S. E. J.; Niemann, R. G.; Peltola, T. A.; Foster, J. M.; Cameron, P. J.; Walker, A. B. Can Slow-Moving Ions Explain Hysteresis in the Current-Voltage Curves of Perovskite Solar Cells? *Energy Environ. Sci.* **2016**, *9*, 1476-1485.
- (6) Meloni, S.; Moehl, T.; Tress, W.; Franckevicius, M.; Saliba, M.; Lee, Y. H.; Gao, P.; Nazeeruddin, M. K.; Zakeeruddin, S. M.; Rothlisberger, U. et al. Ionic Polarization-Induced Current-Voltage Hysteresis in  $\text{CH}_3\text{NH}_3\text{PbX}_3$  Perovskite Solar Cells. *Nat. Commun.* **2016**, *7*, Article No. 10334.
- (7) Manser, J. S.; Christians, J. A.; Kamat, P. V. Intriguing Optoelectronic Properties of Metal Halide Perovskites. *Chem. Rev.* **2016**, *116*, 12956-13008.

- (8) Xiao, Z. G.; Yuan, Y. B.; Shao, Y. C.; Wang, Q.; Dong, Q. F.; Bi, C.; Sharma, P.; Gruverman, A.; Huang, J. S. Giant Switchable Photovoltaic Effect in Organometal Trihalide Perovskite Devices. *Nat. Mater.* **2015**, *14*, 193-198.
- (9) Wang, M.; Lin, S. Anisotropic and Ultralow Phonon Thermal Transport in Organic-Inorganic Hybrid Perovskites: Atomistic Insights into Solar Cell Thermal Management and Thermoelectric Energy Conversion Efficiency. *Adv. Funct. Mater.* **2016**, *26*, 5297-5306.
- (10) Huang, J.; Yuan, Y.; Shao, Y.; Yan, Y. Understanding the Physical Properties of Hybrid Perovskites for Photovoltaic Applications. *Nat. Rev. Mater.* **2017**, *2*, 17042.
- (11) Kerner, R. A.; Rand, B. P. Ionic–Electronic Ambipolar Transport in Metal Halide Perovskites: Can Electronic Conductivity Limit Ionic Diffusion? *J. Phys. Chem. Lett.* **2018**, *9*, 132-137.
- (12) Lai, W.; Haile, S. M. Impedance Spectroscopy as a Tool for Chemical and Electrochemical Analysis of Mixed Conductors: A Case Study of Ceria. *J. Am. Ceram. Soc.* **2005**, *88*, 2979-2997.
- (13) Jasinski, P.; Petrovsky, V.; Suzuki, T.; Anderson, H. U. Impedance Studies of Diffusion Phenomena and Ionic and Electronic Conductivity of Cerium Oxide. *J. Electrochem. Soc.* **2005**, *152*, J27-J32.
- (14) Zhuang, Q.-C.; Wei, T.; Du, L.-L.; Cui, Y.-L.; Fang, L.; Sun, S.-G. An Electrochemical Impedance Spectroscopic Study of the Electronic and Ionic Transport Properties of Spinel  $\text{LiMn}_2\text{O}_4$ . *J. Phys. Chem. C.* **2010**, *114*, 8614-8621.
- (15) Jamnik, J.; Maier, J. Treatment of the Impedance of Mixed Conductors Equivalent Circuit Model and Explicit Approximate Solutions. *J. Electrochem. Soc.* **1999**, *146*, 4183-4188.

- (16) Gonzalez-Pedro, V.; Juarez-Perez, E. J.; Arsyad, W. S.; Barea, E. M.; Fabregat-Santiago, F.; Mora-Sero, I.; Bisquert, J. General Working Principles of  $\text{CH}_3\text{NH}_3\text{PbX}_3$  Perovskite Solar Cells. *Nano Lett.* **2014**, *14*, 888-893.
- (17) Correa-Baena, J. P.; Turren-Cruz, S. H.; Tress, W.; Hagfeldt, A.; Aranda, C.; Shooshtari, L.; Bisquert, J.; Guerrero, A. Changes from Bulk to Surface Recombination Mechanisms between Pristine and Cycled Perovskite Solar Cells. *ACS Energy Lett.* **2017**, *2*, 681-688.
- (18) Chen, B.; Yang, M. J.; Zheng, X. J.; Wu, C. C.; Li, W. L.; Yan, Y. K.; Bisquert, J.; Garcia-Belmonte, G.; Zhu, K.; Priya, S. Impact of Capacitive Effect and Ion Migration on the Hysteretic Behavior of Perovskite Solar Cells. *J. Phys. Chem. Lett.* **2015**, *6*, 4693-4700.
- (19) Coll, M.; Gomez, A.; Mas-Marza, E.; Almora, O.; Garcia-Belmonte, G.; Campoy-Quiles, M.; Bisquert, J. Polarization Switching and Light-Enhanced Piezoelectricity in Lead Halide Perovskites. *J. Phys. Chem. Lett.* **2015**, *6*, 1408-1413.
- (20) Almora, O.; Guerrero, A.; Garcia-Belmonte, G. Ionic Charging by Local Imbalance at Interfaces in Hybrid Lead Halide Perovskites. *Appl. Phys. Lett.* **2016**, *108*, 043903.
- (21) Domanski, K.; Roose, B.; Matsui, T.; Saliba, M.; Turren-Cruz, S. H.; Correa-Baena, J. P.; Carmona, C. R.; Richardson, G.; Foster, J. M.; De Angelis, F. et al. Migration of Cations Induces Reversible Performance Losses over Day/Night Cycling in Perovskite Solar Cells. *Energy Environ. Sci.* **2017**, *10*, 604-613.
- (22) Hoque, M. N. F.; Yang, M. J.; Li, Z.; Islam, N.; Pan, X.; Zhu, K.; Fan, Z. Y. Polarization and Dielectric Study of Methylammonium Lead Iodide Thin Film to Reveal Its Nonferroelectric Nature under Solar Cell Operating Conditions. *ACS Energy Lett.* **2016**, *1*, 142-149.

- (23) Dualeh, A.; Moehl, T.; Tetreault, N.; Teuscher, J.; Gao, P.; Nazeeruddin, M. K.; Gratzel, M. Impedance Spectroscopic Analysis of Lead Iodide Perovskite-Sensitized Solid-State Solar Cells. *ACS Nano* **2014**, *8*, 362-373.
- (24) Senocrate, A.; Moudrakovski, I.; Kim, G. Y.; Yang, T. Y.; Gregori, G.; Gratzel, M.; Maier, J. The Nature of Ion Conduction in Methylammonium Lead Iodide: A Multimethod Approach. *Angew. Chem. Int. Ed.* **2017**, *56*, 7755-7759.
- (25) Yang, T. Y.; Gregori, G.; Pellet, N.; Gratzel, M.; Maier, J. The Significance of Ion Conduction in a Hybrid Organic-Inorganic Lead-Iodide-Based Perovskite Photosensitizer. *Angew. Chem. Int. Ed.* **2015**, *54*, 7905-7910.
- (26) Guillen, E.; Ramos, F. J.; Anta, J. A.; Ahmad, S. Elucidating Transport-Recombination Mechanisms in Perovskite Solar Cells by Small-Perturbation Techniques. *J. Phys. Chem. C* **2014**, *118*, 22913-22922.
- (27) Contreras, L.; Idigoras, J.; Todinova, A.; Salado, M.; Kazim, S.; Ahmad, S.; Anta, J. A. Specific Cation Interactions as the Cause of Slow Dynamics and Hysteresis in Dye and Perovskite Solar Cells: A Small-Perturbation Study. *Phys. Chem. Chem. Phys.* **2016**, *18*, 31033-31042.
- (28) Pydzinska, K.; Karolczak, J.; Kosta, I.; Tena-Zaera, R.; Todinova, A.; Idigoras, J.; Anta, J. A.; Ziolek, M. Determination of Interfacial Charge-Transfer Rate Constants in Perovskite Solar Cells. *ChemSusChem* **2016**, *9*, 1647-1659.
- (29) Raga, S. R.; Qi, Y. B. The Effect of Impurities on the Impedance Spectroscopy Response of  $\text{CH}_3\text{NH}_3\text{PbI}_3$  Perovskite Solar Cells. *J. Phys. Chem. C* **2016**, *120*, 28519-28526.

- (30) Pascoe, A. R.; Duffy, N. W.; Scully, A. D.; Huang, F. Z.; Cheng, Y. B. Insights into Planar CH<sub>3</sub>NH<sub>3</sub>PbI<sub>3</sub> Perovskite Solar Cells Using Impedance Spectroscopy. *J. Phys. Chem. C* **2015**, *119*, 4444-4453.
- (31) Bag, M.; Renna, L. A.; Adhikari, R. Y.; Karak, S.; Liu, F.; Lahti, P. M.; Russell, T. P.; Tuominen, M. T.; Venkataraman, D. Kinetics of Ion Transport in Perovskite Active Layers and Its Implications for Active Layer Stability. *J. Am. Chem. Soc.* **2015**, *137*, 13130-13137.
- (32) Pockett, A.; Eperon, G. E.; Sakai, N.; Snaith, H. J.; Peter, L. M.; Cameron, P. J. Microseconds, Milliseconds and Seconds: Deconvoluting the Dynamic Behaviour of Planar Perovskite Solar Cells. *Phys. Chem. Chem. Phys.* **2017**, *19*, 5959-5970.
- (33) Hoque, M. N. F.; Islam, N.; Li, Z.; Ren, G. F.; Zhu, K.; Fan, Z. Y. Ionic and Optical Properties of Methylammonium Lead Iodide Perovskite across the Tetragonal-Cubic Structural Phase Transition. *ChemSusChem* **2016**, *9*, 2692-2698.
- (34) Yadav, P.; Prochowicz, D.; Alharbi, E. A.; Zakeeruddin, S. M.; Gratzel, M. Intrinsic and Interfacial Kinetics of Perovskite Solar Cells under Photo and Bias-Induced Degradation and Recovery. *J. Mater. Chem. C* **2017**, *5*, 7799-7805.
- (35) van Reenen, S.; Kemerink, M.; Snaith, H. J. Modeling Anomalous Hysteresis in Perovskite Solar Cells. *J. Phys. Chem. Lett.* **2015**, *6*, 3808-3814.
- (36) Zoltowski, P. On the Electrical Capacitance of Interfaces Exhibiting Constant Phase Element Behaviour. *J. Electroanal. Chem.* **1998**, *443*, 149-154.
- (37) Kim, H.-S.; Mora-Sero, I.; Gonzalez-Pedro, V.; Fabregat-Santiago, F.; Juarez-Perez, E. J.; Park, N.-G.; Bisquert, J. Mechanism of Carrier Accumulation in Perovskite Thin-Absorber Solar Cells. *Nat. Commun.* **2013**, *4*, 2242.

- (38) Juarez-Perez, E. J.; Sanchez, R. S.; Badia, L.; Garcia-Belmonte, G.; Kang, Y. S.; Mora-Sero, I.; Bisquert, J. Photoinduced Giant Dielectric Constant in Lead Halide Perovskite Solar Cells. *J. Phys. Chem. Lett.* **2014**, *5*, 2390-2394.
- (39) Tress, W.; Marinova, N.; Moehl, T.; Zakeeruddin, S. M.; Nazeeruddin, M. K.; Grätzel, M. Understanding the Rate-Dependent J–V Hysteresis, Slow Time Component, and Aging in  $\text{CH}_3\text{NH}_3\text{PbI}_3$  Perovskite Solar Cells: The Role of a Compensated Electric Field. *Energy Environ. Sci.* **2015**, *8*, 995-1004.
- (40) Macdonald, D. D. Reflections on the History of Electrochemical Impedance Spectroscopy. *Electrochim. Acta* **2006**, *51*, 1376-1388.
- (41) Ho, C.; Raistrick, I. D.; Huggins, R. A. Application of AC Techniques to the Study of Lithium Diffusion in Tungsten Trioxide Thin Films. *J. Electrochem. Soc.* **1980**, *127*, 343-350.
- (42) Liu, Y.; Renna, L. A.; Thompson, H. B.; Page, Z. A.; Emrick, T.; Barnes, M. D.; Bag, M.; Venkataraman, D.; Russell, T. P. Role of Ionic Functional Groups on Ion Transport at Perovskite Interfaces. *Adv. Ener. Mater.* **2017**, *7*, 1701235.
- (43) Zhang, Y.; Liu, M.; Eperon, G. E.; Leijtens, T. C.; McMeekin, D.; Saliba, M.; Zhang, W.; de Bastiani, M.; Petrozza, A.; Herz, L. M. et al. Charge Selective Contacts, Mobile Ions and Anomalous Hysteresis in Organic-Inorganic Perovskite Solar Cells. *Mater. Horiz.* **2015**, *2*, 315-322.
- (44) Correa-Baena, J.-P.; Anaya, M.; Lozano, G.; Tress, W.; Domanski, K.; Saliba, M.; Matsui, T.; Jacobsson, T. J.; Calvo, M. E.; Abate, A. et al. Unbroken Perovskite: Interplay of Morphology, Electro-Optical Properties, and Ionic Movement. *Adv. Mater.* **2016**, *28*, 5031-5037.
- (45) Levine, I.; Nayak, P. K.; Wang, J. T.-W.; Sakai, N.; Van Reenen, S.; Brenner, T. M.; Mukhopadhyay, S.; Snaith, H. J.; Hodes, G.; Cahen, D. Interface-Dependent Ion

Migration/Accumulation Controls Hysteresis in  $\text{MapbI}_3$  Solar Cells. *J. Phys. Chem. C* **2016**, *120*, 16399-16411.

(46) Joshi, P. H.; Zhang, L.; Hossain, I. M.; Abbas, H. A.; Kottokkaran, R.; Nehra, S. P.; Dhaka, M.; Noack, M.; Dalal, V. L. The Physics of Photon Induced Degradation of Perovskite Solar Cells. *AIP Adv.* **2016**, *6*, 115114.

(47) Wang, P.; Ulfa, M.; Pauporté, T. Effects of Perovskite Monovalent Cation Composition on the High and Low Frequency Impedance Response of Efficient Solar Cells. *J. Phys. Chem. C* **2018**, *122*, 1973–1981.

(48) Gnahn, M.; Pajkossy, T.; Kolb, D. M. The Interface between Au(111) and an Ionic Liquid. *Electrochim. Acta* **2010**, *55*, 6212-6217.

(49) Fedorov, M. V.; Kornyshev, A. A. Ionic Liquid near a Charged Wall: Structure and Capacitance of Electrical Double Layer. *J. Phys. Chem. B* **2008**, *112*, 11868-11872.

(50) Kornyshev, A. A. Double-Layer in Ionic Liquids: Paradigm Change? *J. Phys. Chem. B* **2007**, *111*, 5545-5557.

(51) Franceschetti, D. R.; Macdonald, J. R.; Buck, R. P. Interpretation of Finite-Length-Warburg-Type Impedances in Supported and Unsupported Electrochemical Cells with Kinetically Reversible Electrodes. *J. Electrochem. Soc.* **1991**, *138*, 1368-1371.

(52) Azpiroz, J. M.; Mosconi, E.; Bisquert, J.; Angelis, F. Defect Migration in Methylammonium Lead Iodide and Its Role in Perovskite Solar Cell Operation. *Energy Environ. Sci.* **2015**, *8*, 2118-2127.

(53) Guerrero, A.; You, J.; Aranda, C.; Kang, Y. S.; Garcia-Belmonte, G.; Zhou, H.; Bisquert, J.; Yang, Y. Interfacial Degradation of Planar Lead Halide Perovskite Solar Cells. *ACS Nano* **2016**, *10*, 218-224.



## TOC Graphic

